# Numerical Prediction of Effect of Intake Port Configurations on the Induction Swirl Intensity by Three-Dimensional Gas Flow Analysis

Y. Isshiki, Y. Shimamoto and T. Wakisaka
Department of Mechanical Engineering
Kyoto University
Yoshida, Sakyo-ku, Kyoto

ABSTRACT

This paper describes a method for estimating the induction swirl intensity by means of the numerical simulation of gas flow in the intake ports of four-cycle engines.

Three-dimensional flow of compressible viscous gas in the intake ports has been calculated for intake process in order to predict the effect of the configuration of the intake ports, especially the configuration of the helical ports, on the induction swirl intensity and the volumetric efficiency. The results show that the present method is applicable to analyze the flow in the intake ports and also that the induction swirl intensity and the volumetric efficiency can be estimated from the distribution of the calculated outflow velocity around the intake valve. Furthermore, investigation has been made into the effects of the helical port configuration and the valve head geometry.

## INTRODUCTION

In a direct injection four-cycle diesel engine, the generation of induction swirl which affects the combustion process is controlled by contriving the configuration of the intake port such as the helical port or others. During the trial stage of the intake port designing, the ability to generate swirl is estimated by steady flow test and the optimum port configuration seems to be searched for through the method of trial and error. To test a great number of configurations for the intake port by experiments, however, would take too much time and labor. Therefore in order to develop the intake ports efficiently, the method of computer aided design (CAD), by which the effects of the intake port configuration upon the swirl intensity as well as upon the volumetric efficiency are predicted numerically at the early stage of design, appears to be one of the most efficient means for the future.

With the progress of computer technology and numerical simulation techniques, the numerical analysis of gas motion has become available in the field of internal combustion engines. As for in-cylinder flow, some three-dimensional calculations for intake, compression and scavenging processes have been made (1)-(3). As for intake and exhaust systems, two-dimensional analysis has been made for the flow in the intake manifold as well as the flow in the intake port (4),(5), but there seems to be few examples of the three-dimensional analysis of the flow in the intake port.

The purpose of this study is to predict the relations among the intake port configuration, the swirl intensity and the volumetric efficiency. So the swirl intensity and the volumetric efficiency have been estimated by the three-dimensional numerical analysis of the unsteady flow in the intake port regarding it as compressible viscous fluid. As for the way to represent an arbitrary geometry of a passage, the method of orthogonal or non-orthogonal curvilinear coordinate transformation and the arbitrary Lagrangian-Eulerian (ALE) technique are available. In this study, however, in consideration of easiness to change the wall boundary in making calculations, Cartesian coordinates have been used as a coordinate system and a staircase-like boundary has been used for expressing the wall boundary approximately.

First, in order to examine the accuracy of the method of numerical analysis, the calculated results under steady conditions have been compared with the results of steady flow experiments, And then, applying this method to helical ports, the swirl intensity and the volumetric efficiency have been calculated under a motoring condition and the effects of the intake port configuration and the valve head geometry have been investigated.

## METHOD OF NUMERICAL ANALYSIS

### Intake Port Model and Coordinates

In order to estimate exactly the swirl intensity and the volumetric efficiency it is necessary to analyze the whole process of flow through the intake port and the cylinder. However, the three-dimensional analysis of the whole process is perhaps impractical, considering the time required for calculation and the capacity of a computer. Therefore, in this study the flow in the intake port alone has been analyzed under the adequate boundary conditions. The domain of analysis is restricted to such a passage, which is shown in Fig. 1, as its inlet boundary is the junction between the intake pipe and the cylinder head, and its outlet boundary is the cylindrical part formed between the valve and the valve seat. In a system of Cartesian coordinates (x,y,z), the axis z is set on the valve axis, and the origin is set on the intersecting point of the axis with the plane containing the contact position of the valve seat, as shown in Fig. 1. The axis x is perpendicular to the inlet boundary section.

Considering the easiness to treat the outlet boundary, it seems that the expanding or contracting coordinates are suitably applied to the space between the valve face and the plane x-y containing the origin. However, in the practical case where a comparatively small number of control volumes is used, there may arise some defect that the valve head geometry cannot be expressed adequately only by means of expanding/contracting coordinates. So, in this study the above mentioned space is treated by separating it into the region of the expanding/contracting coordinates and that of the translating coordinates which move in parallel with valve motion.

At the position of the maximum valve lift ⓪ in Fig. 2, the intervals of control volumes along the axis z are set as shown in the left of the figure. The boundary of the valve head drawn with a thick broken line is modeled by a staircase-like boundary drawn with a thick solid line. As the oblique-lined control volumes are within the valve head , only the control volumes which are not oblique-lined are the objects to be calculated. The slabs k1,k2 from the origin 0 to the point $A(z=z_f)$ are treated by the expanding/contracting coordinates, while the slabs k3-k5 from the point A to the valve base $B(z=z_{val})$ are treated by the translating coordinates. The position A on the boundary between these two coordinates moves at the same speed as that of the valve. When the valve reaches the adequate position ①, the boundary between the expanding/contracting coordinates and the translating ones is changed over; from the boundary of the slabs k2, k3 to the boundary of k3, k4. In the same way it is changed over to the boundary of k4, k5 at the position ②. By changing the intervals of control volumes along the axis z according to the valve motion in this way, the number of control volumes available for calculation can be kept so as not to decrease severely in the range of small valve lift, and also the configuration of the valve head can be expressed more appropriately by this method than only using the expanding/ contracting coordinates.

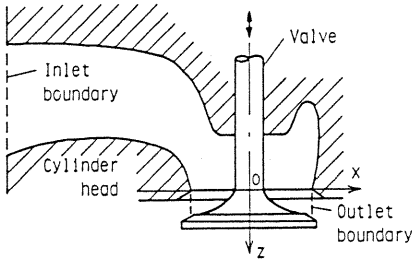


Fig. 1 Schematic of an intake port

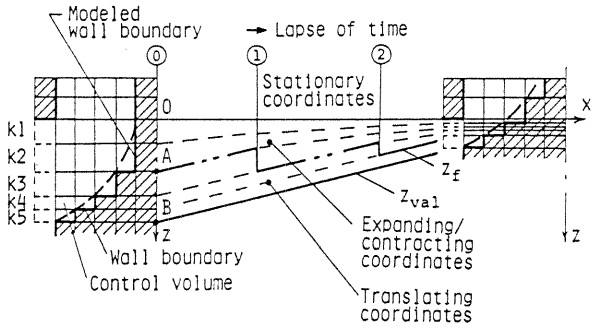


Fig. 2 Relation between valve position and $z_f$

## Fundamental Equations

Assuming that the gas is the compressible viscous fluid conforming to the ideal gas law, the conservation equations of its mass, momentum and energy can be written as,

$$\frac{1}{z_v}\frac{\partial}{\partial t}(\rho\phi z_v)+\frac{\partial}{\partial x}(\rho v_x\phi-\Gamma_\phi\frac{\partial\phi}{\partial x}) +\frac{\partial}{\partial y}(\rho v_y\phi-\Gamma_\phi\frac{\partial\phi}{\partial y}) +\frac{1}{z_v}\frac{\partial}{\partial\zeta}(\rho v_\zeta\phi-\frac{\Gamma_\phi}{z_v}\frac{\partial\phi}{\partial\zeta})=S_\phi \quad (1)$$

where $\phi$ = dependent variable, $\Gamma_\phi$ = effective exchange coefficient of $\phi$, $S_\phi$ = source term for $\phi$. $\phi$, $\Gamma_\phi$ and $S_\phi$ concerning the respective conservation equations are shown in Table 1. $\zeta$, $z_v$ and $v_\zeta$ in Eq. (1) are different in each region as shown in Fig. 2, and they can be expressed as follows:

(1) In the region of stationary coordinates;

$$\zeta=z,\ z_v=1,\ v_\zeta=v_z \quad (2)$$

(2) In the region of expanding or contracting coordinates;

$$\zeta=z/z_f,\ z_v=z_f,\ v_\zeta=v_z-\zeta(dz_f/dt) \quad (3)$$

(3) In the region of translating coordinates;

$$\zeta=1+(z-z_f)/(z_{val}-z_f)$$
$$z_v=z_{val}-z_f,\ v_\zeta=v_z-dz_{val}/dt \quad (4)$$

Table 1 $\phi$, $\Gamma_\phi$, $S_\phi$ for Eq. (1)

| Equation | $\phi$ | $\Gamma_\phi$ | $S_\phi$ |
|---|---|---|---|
| Mass | 1 | 0 | 0 |
| Momentum | $v_x$ | $\mu_e$ | $-\frac{\partial p}{\partial x}+\frac{1}{3}\frac{\partial}{\partial x}(\mu_e \mathrm{div}\ \mathbf{v})$ |
| | $v_y$ | $\mu_e$ | $-\frac{\partial p}{\partial y}+\frac{1}{3}\frac{\partial}{\partial y}(\mu_e \mathrm{div}\ \mathbf{v})$ |
| | $v_z$ | $\mu_e$ | $-\frac{1}{z_v}\frac{\partial p}{\partial\zeta}+\frac{1}{3z_v}\frac{\partial}{\partial\zeta}(\mu_e \mathrm{div}\ \mathbf{v})$ |
| Energy | h | $(\frac{\mu}{\sigma})_e$ | $\frac{\partial p}{\partial t}+v_x\frac{\partial p}{\partial x}+v_y\frac{\partial p}{\partial y}+\frac{v_\zeta}{z_v}\frac{\partial p}{\partial\zeta}$ $+\mu_e[2(e_{xx}^2+e_{yy}^2+e_{\zeta\zeta}^2)$ $+e_{y\zeta}^2+e_{\zeta x}^2+e_{xy}^2-\frac{2}{3}(\mathrm{div}\ \mathbf{v})^2]$ |

Note: $e_{xx}=\frac{\partial v_x}{\partial x}$, $e_{yy}=\frac{\partial v_y}{\partial y}$, $e_{\zeta\zeta}=\frac{1}{z_v}\frac{\partial v_z}{\partial\zeta}$

$e_{y\zeta}=\frac{\partial v_z}{\partial y}+\frac{1}{z_v}\frac{\partial v_y}{\partial\zeta}$

$e_{\zeta x}=\frac{1}{z_v}\frac{\partial v_x}{\partial\zeta}+\frac{\partial v_z}{\partial x}$

$e_{xy}=\frac{\partial v_y}{\partial x}+\frac{\partial v_x}{\partial y}$

$\mathrm{div}\ \mathbf{v}=e_{xx}+e_{yy}+e_{\zeta\zeta}$

$\mu_e=\mu_l+\mu_t$ , $\sigma_l=0.72$

$(\frac{\mu}{\sigma})_e=(\frac{\mu}{\sigma})_l+(\frac{\mu}{\sigma})_t$ , $\sigma_t=0.9$ (7)

where $dz_f/dt = dz_{val}/dt$.

Eddy viscosity $\mu_t$ must be determined on the basis of an adequate turbulence model. Concerning internal combustion engines, there are some examples in which the k-ε model is used (2)(5). In this approach it is comparatively easy to obtain the characteristic values of turbulence. However, not only several empirical constants are required but also two additional partial differential equations must be solved.

On the other hand, there are some examples in which the eddy viscosity employed in the Subgrid Scale (SGS) model is applied to an internal combustion engine (1)(3)(6), though these studies do not come within the category of the Large Eddy Simulation. In such an approach the characteristics of turbulence such as turbulence intensity cannot be obtained, but the required empirical constant is only one and there is no need to solve any additional transport equations.

As the author's major purpose is to calculate the distribution of mean flow velocity and to study the relation between the swirl intensity and the intake port configuration, the eddy viscosity which is determined by the following expression in the SGS model is used in this study;

$$\mu_t=\rho(c_\mu\Delta_c)^2[2(e_{xx}^2+e_{yy}^2+e_{\zeta\zeta}^2)+e_{y\zeta}^2+e_{\zeta x}^2+e_{xy}^2]^{1/2} \quad (5)$$

where $c_\mu$ = empirical constant (= 0.1 (8)), $\Delta_c$ = characteristic size of a control volume = (volume of a control volume)$^{1/3}$.

## Calculation Procedure

The Tank and Tube method (9)(10), i.e., a kind of finite volume method, is used for the numerical analysis of compressible viscous fluid.

The domain for analysis is divided into a number of control volumes of rectangular prism as shown in Fig. 3. Density ρ, pressure p and enthalpy h, which are scalar variables, are the values placed within the control volume shown in Fig. 3(b), while each velocity vector component $v_x$, $v_y$, $v_z$ is placed on each surface of the control volume. Regarding the energy conservation equation ( $\phi$ = h in Eq. (1)), its discritization equation is derived by integrating Eq. (1) over the control volume shown with the solid line. Regarding the momentum equations ($\phi$= $v_x$, $v_y$, $v_z$), their discritization equations are obtained for the control volume staggered by half of the volume from the control volume of h (for example, the $v_x$-control volume is shown with the broken line in Fig. 3(b)). As for the discritization of the convection and diffusion terms in Eq. (1) the hybrid scheme is used, and as for the discritization in time the Crank-Nicolson method is used.

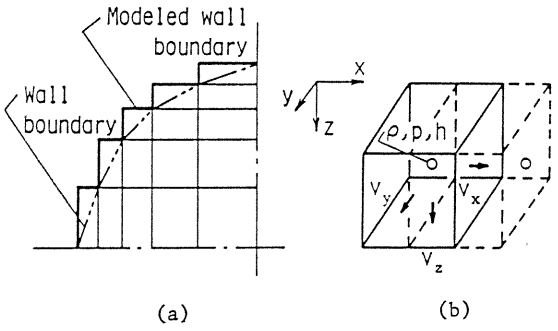


Fig. 3 Division into control volumes

Using the known quantities in a time-step, the discritized conservation equations of momentum and energy are solved to give the velocity components and enthalpy in the next time-step. As the velocity field thus obtained dose not satisfy the mass conservation equation, the velocity components pressure must be corrected to satisfy the mass conservation equation using the correction equation derived from each conservation equations (11). Then density is calculated with the equation of state. As the quantities obtained through the above calculation do not still satisfy the conservation equations of momentum and energy, the calculation needs to be iterated. When the space average of the absolute value of relative residual calculated from each discritization equation becomes less than a permissive error, the calculated result is recognized as a converged solution and the calculation is advanced to the following time-step.

## Initial and Boundary Conditions

In this study, the initial condition at the timing of the intake valve opening is set to be a stationary state in the intake port, and then the calculation is made at every 2.5° crank angle until the intake valve is closed.

As the boundary conditions, the following assumptions are made:

(1) Inlet boundary: If the state of the inlet section is known, it can be used. In this study, however, it is assumed that the pressure in the inlet section is uniform and the velocity direction is perpendicular to the section. When the outer gas (i.e., air) at the atmospheric state flows in through the inlet, it undergoes isentropic change. When the gas flows out, it undergoes constant-pressure process.

(2) Outlet boundary: As for the pressure and temperature in the outlet section, that is, in the cylinder side, the pressure and temperature in the cylinder at each crank angle obtained by the one-dimensional characteristic method (12) are used. The gas flows in parallel with the circular cone of the valve seat. The direction of the gas flowing out in parallel with the valve seat through the outlet is the same as the direction of the flow in the adjoining upstream control volume. When the gas flows backward from the outlet boundary, it flows toward the valve axis in parallel with the valve seat.

(3) Wall boundary: The velocity of gas at the stationary wall is zero. The velocity of gas at the moving valve is the same as that of the valve. The shear stress on the wall is in proportion to the velocity gradient perpendicular to the wall. The temperature of the wall is the same as that of the atmosphere. The temperature of gas at the wall is equal to the wall temperature. The heat flux at the wall is in proportion to the temperature gradient.

## MODEL ENGINE AND MODEL PASSAGES

The main specifications of a model engine are; bore = 130 mm, stroke = 150 mm, compression ratio = 15.6, timing of intake valve opening = 18° BTDC, timing of intake valve closing = 52° ABDC, intake port diameter = 52 mm, valve seat angle = 30°. The valve lift $L_v$ is shown in Fig. 5.

As basic models of the intake ports, the following four types of passages are set up:

(1) Model SP is composed of a straight pipe and a disk (its thickness is assumed to be zero) corresponding to an intake valve without a stem, as shown in Fig. 4(a).
(2) Model RP is composed of a straight pipe, to which a rectangular passage is attached at a right angle, a valve stem and a disk-shaped valve head (its thickness is assumed to be zero), as shown in Fig. 4(b).
(3) Model HP is a helical-type port having the same intake valve as the model RP, as shown in Fig. 4(c).
(4) Model P is a closely imitated model of a practical helical-type port, as shown in Fig. 4(d). This model also has the same intake valve as the model RP.

The model SP, which is a simplified intake port, is used to examine whether the unsteady flow can be calculated by the above-mentioned method of numerical analysis. The model RP and the model HP are employed for comparing the calculated results with the experimental results under the steady conditions and examining the accuracy of the numerical method used in this study. The model HP is also employed to calculate the swirl ratio under the motoring condition. The model P is used to investigate the effects of the passage configuration and the valve head geometry on the swirl ratio and the volumetric efficiency under the motoring condition.

## EXAMINATION OF ACCURACY

### Preliminary Calculation of Unsteady Flow

The unsteady flow in the model SP under the motoring condition at an engine speed of 30 $s^{-1}$ has been calculated using the cylinder pressure $p_c$ computed by the one-dimensional characteristic method for this model passage. The curve of $p_c$ normalized by the atmospheric pressure $p_a$ is shown in Fig. 5. Figure 6 shows the mass flow rate m and the volumetric efficiency $\eta_v$ obtained from the calculated velocity and density on the outlet boundary. For the purpose of comparison, the results obtained by the one-dimensional analysis are also shown in this figure. As the values of m and $\eta_v$ calculated by each method nearly coincide with each other, it is found that this three-dimensional method can give the flow rate characteristics under the nearly actual pressure condition.

Figure 7 shows an example of velocity distribution on the outlet boundary at the approximately middle position of the valve lift. Each arrow in the figure indicates the resultant velocity of $v_x$ and $v_y$, that is, the velocity vector projection on the plane x-y. Because the outflow is uniformly radiated from the outlet boundary, it seems that there are no noticed errors resulting from representing a cylindrical port by staircase-like boundary. Therefore, this three-dimensional calculation presumably leads to a fairly valid flow field.

### Comparison with Experimental Results

Fig. 8(a) shows the experimental apparatus. A test port and a valve (shown in Fig.8(b)) were installed on an acrylite cylinder having the same diameter as that of the model engine cylinder. By sucking the air with a blower, a constant pressure difference $\Delta p$ was generated between the atmosphere and the inside of the cylinder. The flow rate was measured with an orifice, and the discharge coefficient $C_d$ was calculated from the flow rate and the pressure difference on the basis of the

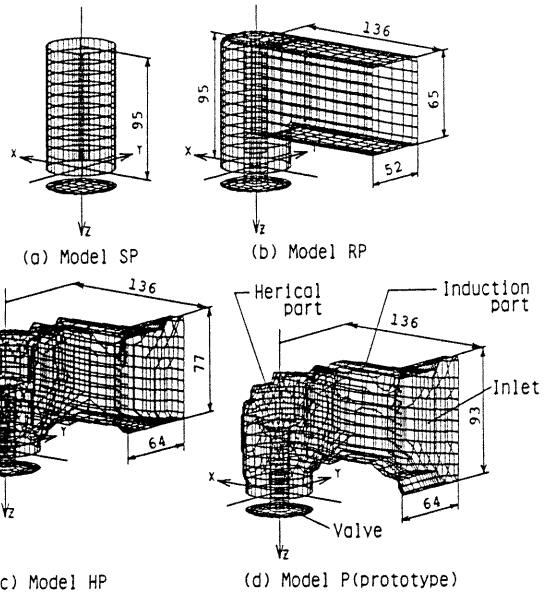


Fig. 4 Models of passage

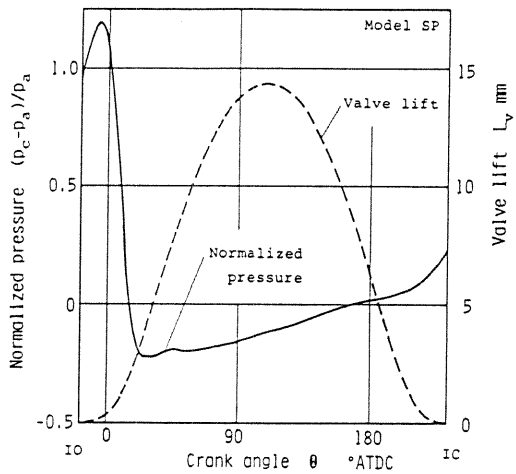


Fig. 5 Valve lift and the pressure in the cylinder
IO = intake opening, IC = intake closing

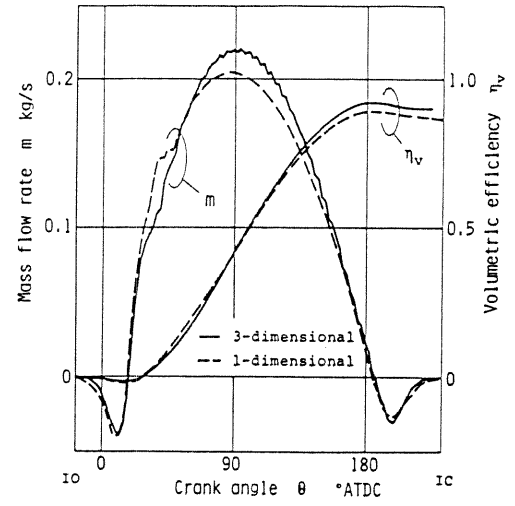


Fig. 6 Mass flow rate and volumetric efficiency for model SP under motoring condition

cross-sectional area between the valve and the valve seat, $F_v$, which is given by the following expression;

$$F_v=\pi L_v \cos\theta_v (d+L_v \cos\theta_v \sin\theta_v) \qquad (6)$$

where $L_v$ = valve lift, $\theta_v$ = valve seat angle, d = intake port diameter.

The outflow velocity around the valve was measured with a hot-wire probe (a tungsten element of 5 μm in diameter and 1.2 mm in length) inserted into the gap between the valve and the valve seat, as shown in Fig. 8(b), at a position $h_p$ on the outlet boundary section. From the outputs of a hot-wire anemometer measured at three different angular positions by turning the probe around its axis, three velocity components of a velocity vector were calculated (13). On its occasion, the flow direction was checked with a tuft. The outflow velocity distribution around the valve was measured by leaving the probe fixed and rotating the test port on the cylinder around the valve axis.

The experiment was made on the model RP and the model HP. In the calculation, setting the stationary state as the initial state for the time-marching calculation, a steady-state solution has been obtained for the same valve lift and pressure difference as in the experiment.

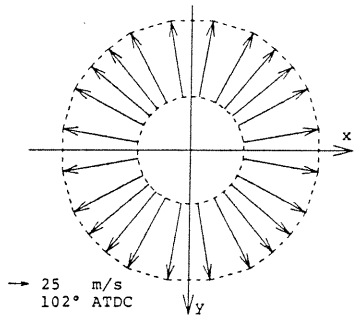


Fig. 7 Outlet velocity distribution for model SP under motoring condition

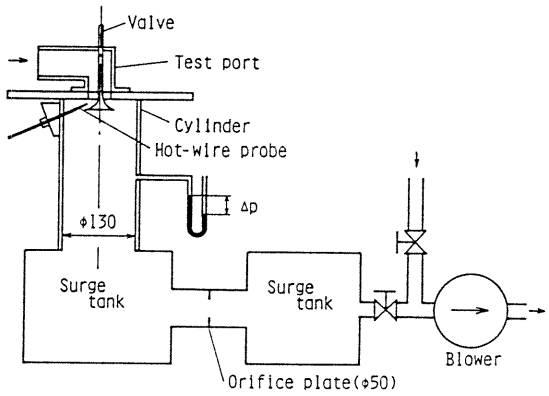


(a) Flow bench schematic

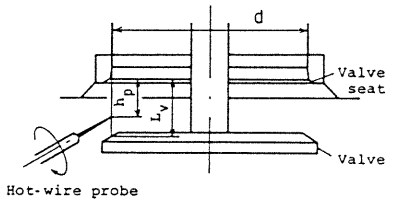


(b) Schematic of the probe setup

Fig. 8 Schematic of the experimental apparatus

Figure 9 shows the experimental and calculated values of $C_d$ for the model RP under the condition of pressure difference of 2.06 kPa. In the vicinity of the maximum valve lift $L_v/d$ of 0.275, the calculated value coincides comparatively well with the experimental one. As the valve lift decreases, however, the difference between them becomes large. Further, when $L_v/d$ is about 0.13, the experimental value changes discontinuously. This discontinuous change is presumed to be due to the abrupt change of flow pattern in the gap between the valve and the valve seat (14). It is not easy to simulate such a phenomenon by calculation because of the difficulty in setting the outlet boundary conditions precisely. It may be said, however, that the general tendency of the change of $C_d$ with the valve lift has been simulated.

Figure 10 shows the comparison between the experimental and calculated values of $C_d$ in the case of the model HP. Through all the range of the valve lift, the calculated values are smaller than the experimental ones. As compared with Fig. 9, it is seen that errors become large when the configuration of the passage becomes complicated. The cause is supposed to be that the number of control volumes is small (about 3200).

Under the condition of the maximum valve lift $L_v$ of 14.3 mm and the pressure difference of 1.13 kPa, the outflow velocity distribution was measured for the model HP at the hot-wire probe position $h_p$ of every 2 mm from 3 mm to 13 mm in the direction of the valve axis. Figure 11(a) shows the velocity vector projections averaged in the direction of the valve axis. In this figure,

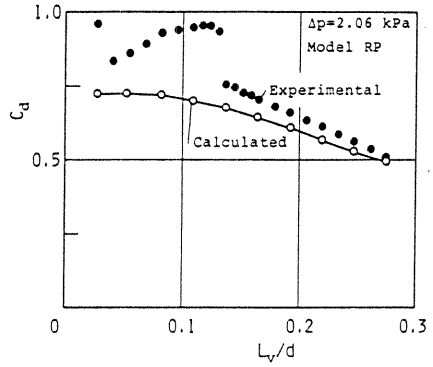


Fig. 9 Relation between the normalized valve lift and the discharge coefficient for model RP under steady condition

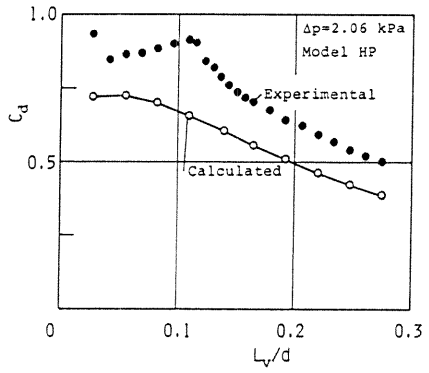


Fig. 10 Relation between the normalized valve lift and the discharge coefficient for model HP under steady condition

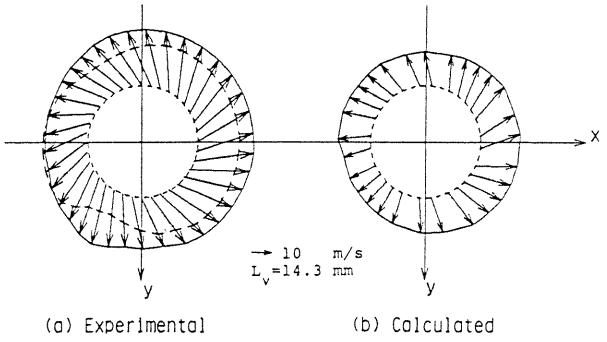


Fig. 11 Outlet velocity distribution for model HP under steady condition

the distribution of the velocity component in the direction of the valve axis is also drawn with a broken line. Alternatively shown in Fig. 11(b) is the calculated velocity distribution (averaged one) on the outlet boundary. The magnitudes of the calculated velocity vector projections are smaller than the experimental ones; this corresponds to the fact that the calculation yields smaller flow rate than the experiment. Figure 11 shows that the calculated velocity vectors twist counter-clockwise in the same way as the experimental ones. By checking the results in detail, it is found that the twisting angles of the vectors are a little smaller in the calculated result than in the experimental one and the pattern of the velocity distribution is somewhat different. It seems that an error is caused by the assumption made as to the boundary conditions; it is assumed that the gas flows out in parallel with the valve seat, although the actual flow direction is not necessarily parallel with the valve seat as shown in Fig. 11(a). It is found in Fig. 11(b), however, that the velocity in the positive side of x is a little larger than that in the negative side of x, as is the same tendency as in the experimental result. From the above-mentioned facts, it may be said that the calculation has simulated comparatively well the general characteristics of the measured outflow velocity distribution.

Swirl Estimation

Supposing that the moment of momentum around the cylinder axis, which the gas flowing out through the outlet boundary has, is equal to the change of the angular momentum caused in the cylinder, the swirl intensity can be estimated from the velocity distribution on the outlet boundary. For the case that the intake valve has an eccentricity ($E_x$ = 9 mm, $E_y$ = 31.5 mm) to the cylinder center as shown in Fig. 12, the following definitions are made: $v_{xy}$ is the resultant velocity in the plane x-y at a point P on the outlet boundary and $r_c$ is the length of a perpendicular from the center of the cylinder, $O_c$, to the vector $v_{xy}$. $v_r$ is the velocity component perpendicular to the outlet boundary surface and ds is the infinitesimal area on the outlet boundary. Then, the angular momentum around the cylinder axis, which is supplied into the cylinder in a unit time, is expressed as

$$\Omega_C = \int_s \rho v_r v_{xy} r_c ds \quad . \tag{7}$$

Therefore, the swirl ratio Sc at any crank angle Θ becomes

$$S_C = \int_{\Theta_{IO}}^{\Theta} \frac{\pi}{180\omega_e} \Omega_C d\Theta \Big/ \frac{\omega_e}{2} R_c^2 M(\Theta) \tag{8}$$

where $\Theta_{IO}$ = timing of intake valve opening, $\omega_e$ = angular speed of engine, $R_c$ = cylinder radius, $M(\Theta)$ = mass of the cylinder contents at crank angle Θ.

Figure 13 shows the swirl ratio $S_c$ which has been obtained with Eq. (8) from the outflow velocity distribution calculated for the model HP under the motoring condition. For the purpose of comparison, calculation has been made of the three-dimensional in-cylinder flow in the model engine, where the calculated velocity distribution around the intake valve for the model HP has been applied as the inflow boundary condition, using the code for in-cylinder flow simulation (1). Then, the swirl ratio $S_{cyl}$ has been obtained with the following expression:

$$S_{cyl} = \int_0^{\xi_p} \int_0^{2\pi} \int_0^{R_c} \rho r^2 v_\theta dr d\theta d\xi \Big/ \omega_e \int_0^{\xi_p} \int_0^{2\pi} \int_0^{R_c} \rho r^3 dr d\theta d\xi \tag{9}$$

where r,θ,ξ = radial, circumferential and axial coordinates, $\xi_p$ = distance between the cylinder head surface and the upper surface of flat piston, $v_\theta$ = circumferential velocity component in the cylinder. The swirl ratio $S_{cyl}$ is shown in Fig. 13. From this figure, it is found that the values of $S_c$ and $S_{cyl}$ are nearly the same. This implies that the decay of swirl is small in the induction

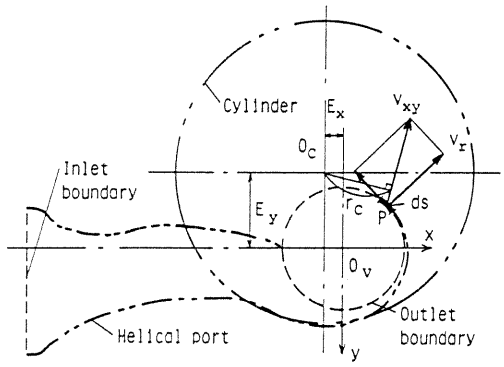


Fig. 12 Schematic of the helical port and the cylinder

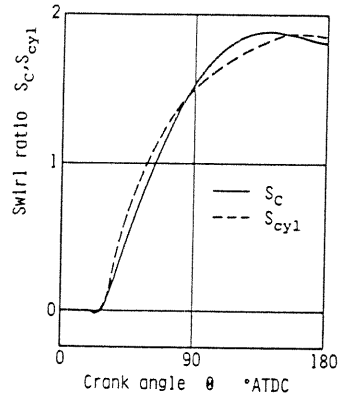


Fig. 13 Swirl ratios for model HP under motoring condition

process and so the angular momentum is conserved. Therefore, Eqs. (7) and (8) can be used for estimating the swirl ratio in the cylinder during the induction process from the velocity distribution around the intake valve.

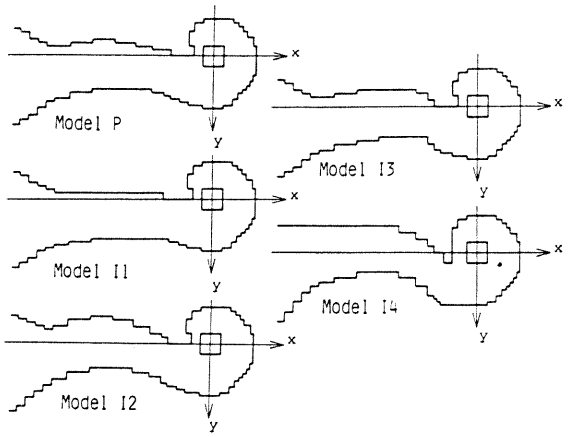


Fig. 14 Variations of the induction part configuration

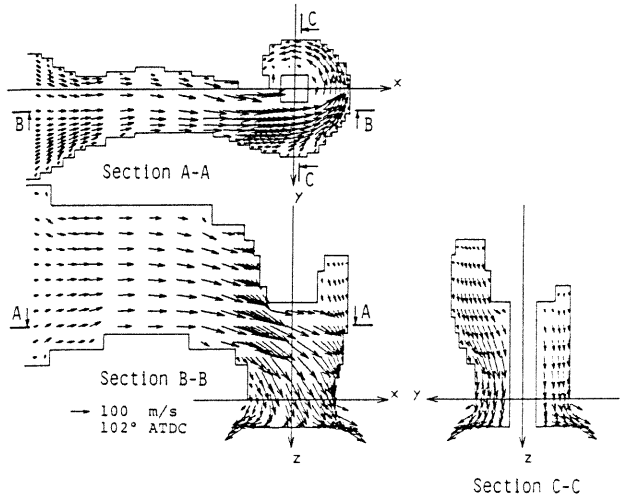


Fig. 15 Velocity vector projections for model P under motoring condition

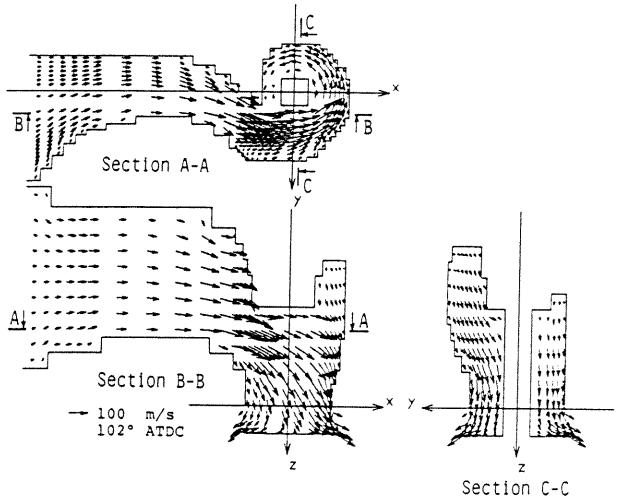


Fig. 16 Velocity vector projections for model I4 under motoring condition

## EFFECT OF INTAKE PORT CONFIGURATION

### Effect of Induction Part Configuration

Figure 14 shows other four models which are derived from the original helical-port model P by varying gradually the shape of the induction part (see Fig. 4(d)), i.e., the part from the inlet to the junction with the helical part (i.e., the part above the valve). In order to compare the flow characteristics in these models easily with each other, the pressure calculated for the model P under the motoring condition at an engine speed of 30 $s^{-1}$ has been applied as the outlet boundary pressure in common with every model.

Figures 15 and 16 exemplify the velocity distribution calculated for the model P and the model I4 at $\Theta = 102°$ where the valve lift becomes nearly maximum. It is found that the flow pattern in the section A-A differs between these models.

Figure 17 shows the outlet velocity distribution, which is averaged in the direction of the valve axis, for the models P and I4. The shapes of the velocity distributions in these two models are almost similar to each other but the magnitudes of the velocity vector projections are smaller in model I4 than in model P. By checking it in detail in the figure, it is found that the twisting angles of the velocity vectors are a little larger in the model I4 than in the model P. Thus, the change of the passage configuration obviously affects the outlet velocity distribution.

Figure 18 shows the swirl ratio $S_c$ and the volumetric efficiency $\eta_v$ at the timing of valve closing for each model shown in Fig. 14.

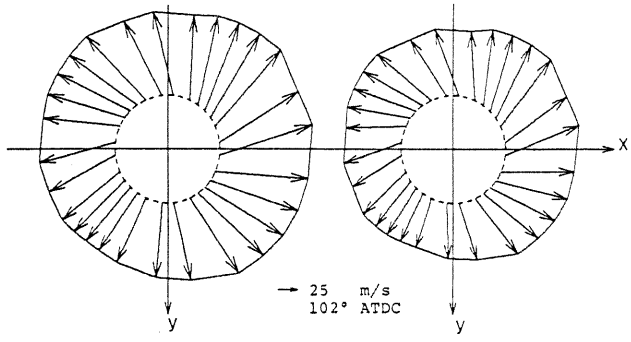


(a) Model P (b) Model I4

Fig. 17 Outlet velocity distribution for models P and I4 under motoring condition

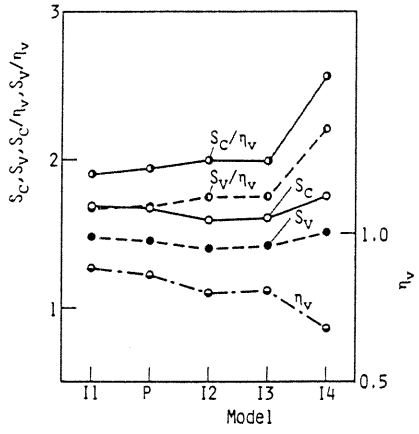


Fig. 18 Effect of the induction part configuration on the swirl ratios and the volumetric efficiency under motoring condition

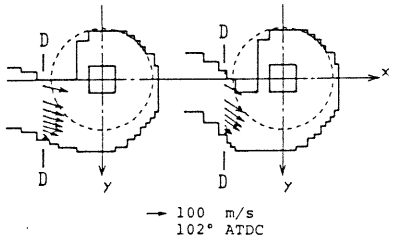


(a) Model P (b) Model I4

Fig. 19 Velocity vector projections at the section D-D under motoring condition

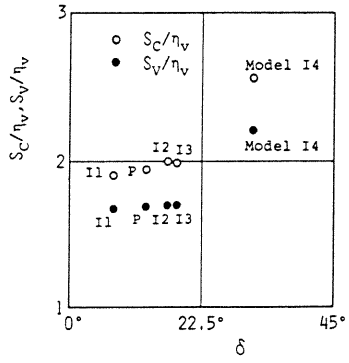


Fig. 20 Relation between the inflow angle and the swirl ratios under motoring condition

Considering that $S_C$ changes according to the eccentricity of the valve center, the swirl ratio in the case of a concentric valve ($E_X = E_Y = 0$ in Fig. 12), $S_V$, is also presented in the same figure. As the outlet velocity distribution for each model is not uniform around the valve axis, as is obvious in Fig. 17, there exists the difference between $S_C$ and $S_V$ due to such ununiformity. From the fact that the difference between $S_C$ and $S_V$ is almost constant in Fig. 18, it is considered that the ununiformity in the outlet velocity distribution is nearly the same for each model.

The volumetric efficiency decreases in the order of the models I1, P, I3, I2 and I4. This seems due to the decrease in the minimum cross section of the passage resulting from the change in the curvature of the induction part. In this way, as the volumetric efficiency is different from model to model, this difference affects the swirl ratios $S_C$ and $S_V$. As $S_C$ and $S_V$ are considered to be approximately proportional to the volumetric efficiency, these are divided by $\eta_v$ to eliminate the influence of $\eta_v$; the modified swirl ratios $S_C/\eta_v$ and $S_V/\eta_v$ are also shown in Fig. 18. As to the model I4, $S_C/\eta_v$ and $S_V/\eta_v$ are considerably large as compared with the other models. Figure 19 shows the velocity on the plane (section D-D), where the gas flows from the induction part into the helical part, for the models P and I4. Arrows in the figure indicate the velocity vector projections averaged in the direction of the axis z. The directions of the velocity vector projections are different between the two models, and the velocity vector projections of the model I4 make a larger angle (this angle is designated $\delta$) with axis x than those of the model P. Figure 20 shows the relation between the averaged value of the angle $\delta$ and the values of $S_C/\eta_v$ and $S_V/\eta_v$. From this figure, it is found that as the angle of inflow into the helical part increases, $S_C/\eta_v$ and $S_V/\eta_v$ increase as well.

Effect of Helical Part Configuration

Figure 21 shows other four models which are derived from the original helical-port model P by varying gradually the height of the helical part (see Fig. 4(d)). Models are numbered in such order as the height of the helical part is lowered. The same pressure is applied on the outlet boundary as that used in the foregoing examination on the induction part. Figure 22 shows the swirl ratios $S_C$ and $S_V$, the volumetric

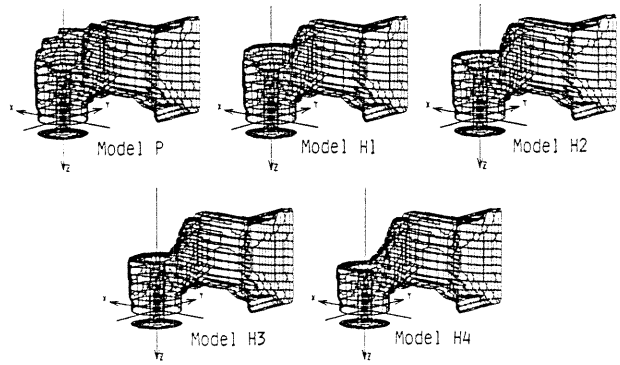


Fig 21 Variations of the helical part configuration

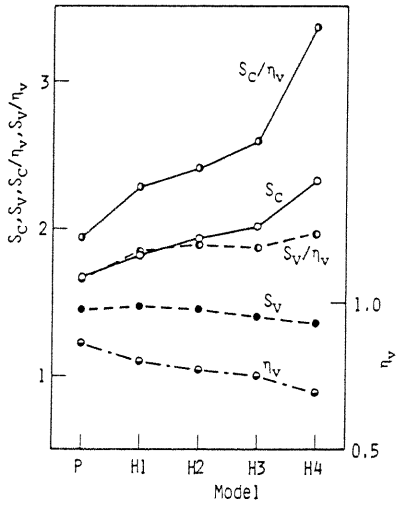


Fig. 22 Effect of the helical part configuration on the swirl ratios and the volumetric efficiency

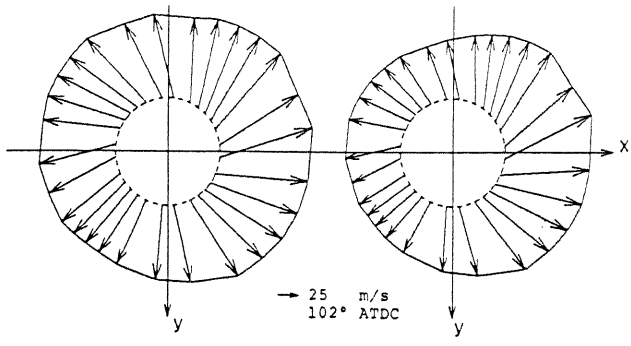


(a) Model P (b) Model H4

Fig. 23 Outlet velocity distribution for models P and H4 under motoring condition

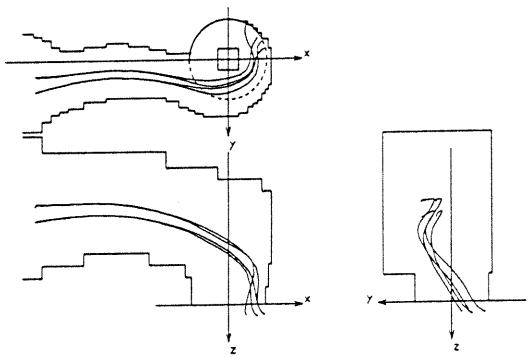

Fig. 24 Traces of gas particles for model P under motoring condition

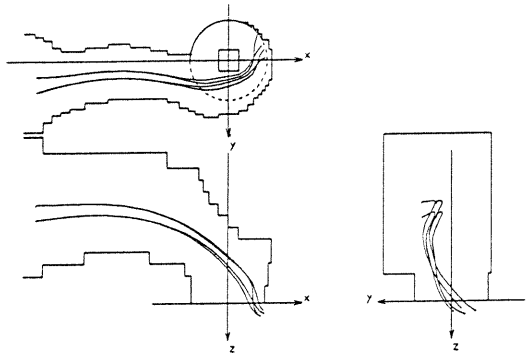

Fig. 25 Traces of gas particles for model H4 under motoring condition

efficiency $\eta_v$ and the modified swirl ratios $S_c/\eta_v$ and $S_v/\eta_v$ for each model. As the height of the helical part becomes lower and so the passage becomes narrower, the volumetric efficiency is getting smaller in the order of the models P, H1, H2, H3 and H4. Also from the figure, it is noticed that $S_c$ becomes larger and the difference between $S_c$ and $S_v$ becomes larger as the height of the helical part gets lower. The outlet velocity distribution at $\theta = 102°$ is shown in Fig. 23 for the models P and H4. The outflow velocity in the model H4 is lower than that of the model P, especially on the negative side of x, so that the velocity distribution is increasingly ununiform. It seems that this leads to the increasing difference between $S_c$ and $S_v$.

Figures 24 and 25 represent the traces of four particles of gas starting at $\theta = 30°$ from the middle positions of the section parallel with the inlet section in the models P and H4. Comparing the traces of particles in the helical part between these models, it is found that in the case of the model P, the particles flow out after changing their direction downward just before the wall in the positive side of x, while in the case of the model H4 the particles flow through without colliding with the wall, due to the influence of the upper portion of the helical part. It is considered that such a difference in the flow pattern causes the aforementioned difference in the outlet velocity distribution.

Effect of Valve Head Geometry

The discharge coefficient $C_d$ was measured under the steady state using the passage of the model RP equipped with one of the three types of the valves D, P and C shown in Fig. 26, in order to compare its result with the result of calculation. The valve D is the same valve as that in Fig. 8(b). The valve P is a practical valve and the model having this valve is designated model RP-P. The valve C is the one with a conical valve head and the model having this valve with the inclination angle $\alpha$ of 45° is designated model RP-C45. Figure 27 shows the relation between the valve head geometry and the discharge coefficient $C_d$. It is found that the calculated value of $C_d$ slightly decreases with the increase of the valve head thickness and such a change of $C_d$ coincides qualitatively with the experimental result.

The effects of the valve head geometry on the swirl ratio and the volumetric efficiency are examined using the passage of the prototype model P and the valve C whose inclination angle $\alpha$ is changed from 0° to 45° (i.e., Models P, P-C15, P-C30 and P-C45). Calculation is made under the motoring condition, applying the same pressure on the outlet boundary as that used in examining the effect of the passage configuration. The swirl

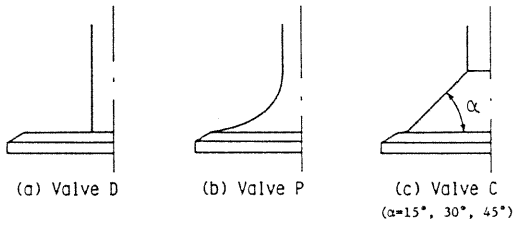


Fig. 26 Models of intake valve

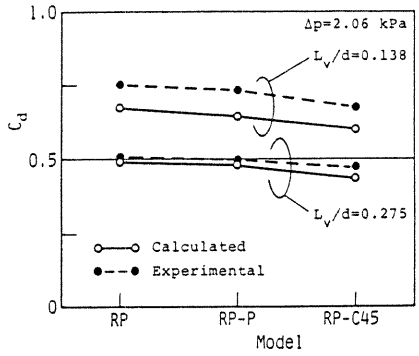


Fig. 27 Relation between the valve head geometry and the discharge coefficient under steady condition

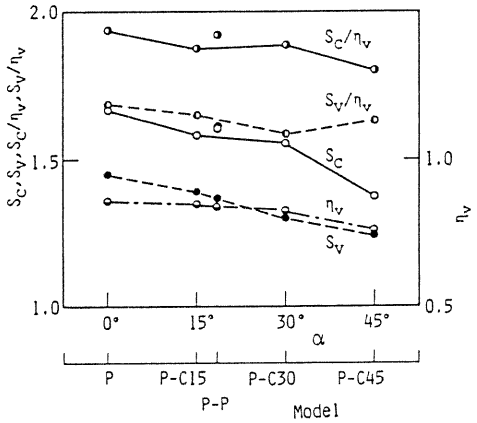


Fig. 28 Effect of the valve head geometry on the swirl ratios and the volumetric efficiency under motoring condition

ratios and the volumetric efficiency are plotted versus the inclination angle in Fig. 28. The calculated results for the model P-P (i.e., the model composed of the passage of the model P and the valve P) are also plotted in this figure, where the averaged inclination of the valve head is taken as $\alpha$. The value of $\eta_V$ becomes small with the increase of $\alpha$. Such tendency corresponds to the aforementioned result of the steady flow experiment. The swirl ratio for the eccentric valve, $S_c$, decreases with the increase in $\alpha$. This decrease, however, includes the influence of the decrease in $\eta_V$, and so attention is paid to the modified swirl ratio $S_c/\eta_V$. It is found that the modified swirl ratio has a tendency to decrease a little with the increase in $\alpha$, that is, with the increase in the valve head thickness.

## CONCLUSIONS

The three-dimensional numerical method for analyzing the compressible, viscous, unsteady flow has been applied to the prediction of gas motion in the practical helical ports. After the validity of the calculation method has been examined by comparing the calculated results with the experimental results under the steady conditions, investigation has been made into the effects of the intake port configuration and the valve head geometry on the induction swirl intensity and the volumetric efficiency. The results obtained are as follows:

(1) The characteristics of induction swirl generation for any intake port having arbitrary configuration may be approximately estimated by this three-dimensional numerical method.

(2) When the angle of inflow into the helical part of the helical port model is made large by changing the configuration of the induction part, the swirl ratio which is modified to eliminate the influence of the volumetric efficiency becomes large.

(3) When the height of the helical part is made low, the swirl ratio becomes large due to the increase in the ununiformity of the outlet velocity distribution, though the volumetric efficiency decreases.

(4) Both of the swirl ratio and the volumetric efficiency slightly decrease with the increase in the thickness of the valve head.

## NOMENCLATURE

$c_p$ = specific heat at constant pressure
$h$ = enthalpy ( $=c_pT$ )
$p$ = pressure
$T$ = temperature
$t$ = time
$\mathbf{v}$ = velocity vector
$v_x, v_y, v_z$ = velocity vector components
$x, y, z$ = Cartesian coordinates
$\theta$ = crank angle from TDC of intake stroke
$\mu$ = viscosity
$\rho$ = density
$\sigma$ = Prandtl number

Subscripts
$e$ = effective
$\ell$ = laminar
$t$ = turbulent

## ACKNOWLEDGMENT

This work has been partially supported by the Scientific Research of a Grant-in-Aid from the Ministry of Education of Japanese Government. The calculation was carried out by Kyoto University Computer FACOM VP-100.

## REFERENCES

1. Wakisaka, T., Shimamoto, Y., Isshiki, Y. and Shibata, T., "Numerical Simulation of Gas Flow in the Cylinders of Four-Stroke Cycle Engines(1st Report)", (in Japanese), Prepr. of 4th Joint Symposium on Internal Combustion Engines, pp. 55-60, 1984.
2. Gosman, A. D., Tsui, Y. Y. and Watkins, A. P., "Calculation of Three Dimensional Air Motion in Model Engines", SAE Paper, No. 840229, 1984.
3. Adachi, T., Kato, S. and Tsujimura, H., "Numerical Analysis of Scavenging Flow in Two-Cycle Internal combustion Engine", ASME Meeting on Flows in Internal Combustion Engines, pp. 29-34, 1982.
4. Chapman, M., "Two Dimensional Numerical Simulation of Inlet Manifold Flow in a Four Cylinder Internal Combustion Engine", SAE Paper, No. 790244, 1979.
5. Demirdzic, I., Gosman, A. D. and Issa, R. I., "A Finite-Volume Method for the Prediction of Turbulent Flow in Arbitrary Geometries", 7th Int. Conf. on Numerical Methods in Fluid Dynamics, (Reynolds, W. C. and MacCormack, R. W. ed.) Springer Verlag, pp. 144-150,1980.
6. Cloutman, L. D., Dukowicz, J. K., Ramshaw, J. D. and Amsden, A. A., "CONCHAS-SPRAY: A Computer Code for Reactive Flows with Fuel Sprays", Report LA-9294-MS, Los Alamos National Laboratory, 1982.
7. Gosman, A. D., Johns, R. J. R. and Watkins, A. P., "Development of Prediction Methods for In-Cylinder Processes in Reciprocating Engines", Combustion Modeling in Reciprocating Engines, (Mattavi, J. N. and Amann, C. A. ed.), Plenum Press, pp. 69-129, 1980.
8. Deardorff, J. W., "A Numerical Study of Three-Dimensional Turbulent Channel Flow at Large Reynolds Numbers", J. Fluid Mech., Vol. 41, Pt. 2, pp. 453-480, 1970.
9. Gosman, A. D. and Ideriah, F. J. K., "A Computer Program for the Calculation of Two-Dimensional (Plane or Axisymmetrical) Turbulent Recirculating Flows", Mech. Engrg. Dept. Report, Imperial College of Science and Technology, 1976.
10. Pun, W. M. and Spalding, D. B., "A General Computer Program for Two-Dimensional Elliptic Flows", Report HTS/76/2, Mech. Engrg. Dept., Imperial College of Science and Technology, 1976.
11. Patankar, S. V., Numerical Heat Transfer and Fluid Flow, McGraw-Hill, pp. 124-131, 1980.
12. Shimamoto, Y., Oka, M. and Tanaka, Y., "A Research on Inertia Charging Effect of Intake System in Multi-Cylinder Engines", Bull. JSME, Vol. 21. No. 153, pp. 502-510, 1978.
13. Catania, A. E., "3-D Swirling Flows in an Open-Chamber Automotive Diesel Engine with Different Induction Systems", ASME Meeting on Flows in Internal Combustion Engines, pp. 53-66, 1982.
14. Kastner, L. J., Williams, T. J. and White, J. B., "Poppet Inlet Valve Characteristics and their Influence on the Induction Process", Proc. Instn. Mech. Engrs., Vol. 178, Pt.1, No. 36, pp. 955-975, 1963-64.